The role of quasi-plasticity in the extreme contact damage tolerance of the stomatopod dactyl club

Shahrouz Amini[1], Maryam Tadayon[1], Sridhar Idapalapati[2] and Ali Miserez[1,3]★

The structure of the stomatopod dactyl club—an ultrafast, hammer-like device used by the animal to shatter hard seashells—offers inspiration for impact-tolerant ceramics. Here, we present the micromechanical principles and related micromechanisms of deformation that impart the club with high impact tolerance. By using depth-sensing nanoindentation with spherical and sharp contact tips in combination with post-indentation residual stress mapping by Raman microspectroscopy, we show that the impact surface region of the dactyl club exhibits a quasi-plastic contact response associated with the interfacial sliding and rotation of fluorapatite nanorods, endowing the club with localized yielding. We also show that the subsurface layers exhibit strain hardening by microchannel densification, which provides additional dissipation of impact energy. Our findings suggest that the club's macroscopic size is below the critical size above which Hertzian brittle cracks are nucleated.

Structure–property relationships of a wide range of biological hard tissues that have been investigated in the past two decades[1,2], including nacre[3], mollusc shells[4,5], and fish and gastropod armours[6,7], provide a source of inspiration for the fabrication of artificial, tough organic–inorganic composites[8,9]. In comparison with these biomineralized composites, which play a passive (defensive) mechanical role, the stomatopod's (commonly called mantis shrimps) dactyl clubs are dynamically active, hammer-like devices. Exploiting their outstanding vision[10] to accurately target their prey, mantis shrimps deliver fast and powerful punches with their dactyl clubs to shatter the prey's hard shells through repetitive impact loading. Remarkably, these shells are themselves considered a benchmark of supertough biocomposites (Fig. 1). Recent studies[11,12] have correlated the key chemical, as well as the nano- and microstructural features of stomatopod dactyl clubs with their nanomechanical response, revealing that the club is essentially made of two distinct regions: an outer (impact) region and an internal (periodic) region. The outer region exhibits spatially inverted gradients of amorphous calcium carbonate and calcium phosphate in the form of fluorapatite[12] (FAP). FAP gradually changes from an amorphous to a crystalline state towards the outer surface, and this transition is facilitated by templating from calcium sulphate[12]. In addition, crystalline FAP is preferentially oriented towards the outermost club surface to maximize impact forces. On the other hand, the inner region is made of a helicoidal structure composed of partially mineralized chitin fibrils, where the mineral phase is mostly amorphous calcium carbonate.

Although compelling details of the structural design and mechanical properties of the stomatopod clubs have recently emerged, the main contact damage mechanisms and their relative contributions to the contact resistance of the clubs have not been explored. Here, we sought to establish and quantify the contact damage tolerance of stomatopod dactyl clubs using complementary nanomechanical and spectroscopic methods. Notably, our data show that the outer impact layers exhibit a quasi-plastic response related to interfacial sliding and rotation of FAP crystals, whereas the inner soft layers feature strain-hardening behaviour associated with microchannel densification. These mechanisms synergistically combine to enhance the overall damage tolerance of stomatopod dactyl clubs. Critically, brittle Hertzian cracks that would lead to catastrophic cracking of the clubs are prevented during impact because the club size remains below a critical size, below which the contact mechanics response is in the quasi-plastic regime.

Hertzian contact response

Visual inspection of a pristine (freshly produced) club following moulting, and of a repeatedly impacted club, are shown in Fig. 1c. Clear differences in their surface appearance are indicated. The impact surface of used clubs exhibited significant erosion, whereas fresh ones were much more even. We subjected clubs to X-ray microtomography (microCT), which distinctly showed a high surface roughness for the heavily used club (Fig. 1d). On microCT sections of clubs that were heavily impacted, irregularities and depressions were noticed on the surface, whereas cross-sections of pristine samples indicated a smooth and regular curvature.

Stomatopod clubs were probed by nanoindentation with a blunt (cono-spherical) tip in the zz and yy directions normal and parallel to the free impact surface, respectively (Fig. 2a). Critically, spots in the immediate vicinity from one another ($\pm 2 \, \mu m$) were probed across mutually orthogonal directions, as described in the Methods. Load–displacement curves from the impact surface to the bulk (inner layers) are shown in Fig. 2b (yy direction) and in Supplementary Fig. 1 (comparison between both directions). Stress–strain curves were obtained by conducting full unloading cycles at regular load increments according to a procedure described previously[13] (Supplementary Fig. 2 and Supplementary Note 1). The stress values hereafter reported thus correspond to the mean contact pressure P_m and the indentation stress–strain responses derived from this analysis are plotted in Fig. 2c (dry conditions, yy direction) and Fig. 2d (comparison between zz and yy direction). In the outer region the club exhibited a clear elastic–plastic transition with a gradual drop in yield stress (σ_y) moving from

[1]School of Materials Science and Engineering, Nanyang Technological University, 50 Nanyang Avenue, Singapore 639798, Singapore. [2]School of Mechanical & Aerospace Engineering, Nanyang Technological University, 50 Nanyang Avenue, Singapore 639798, Singapore. [3]School of Biological Sciences, Nanyang Technological University, 60 Nanyang Drive, Singapore 637551, Singapore. *e-mail: ali.miserez@ntu.edu.sg
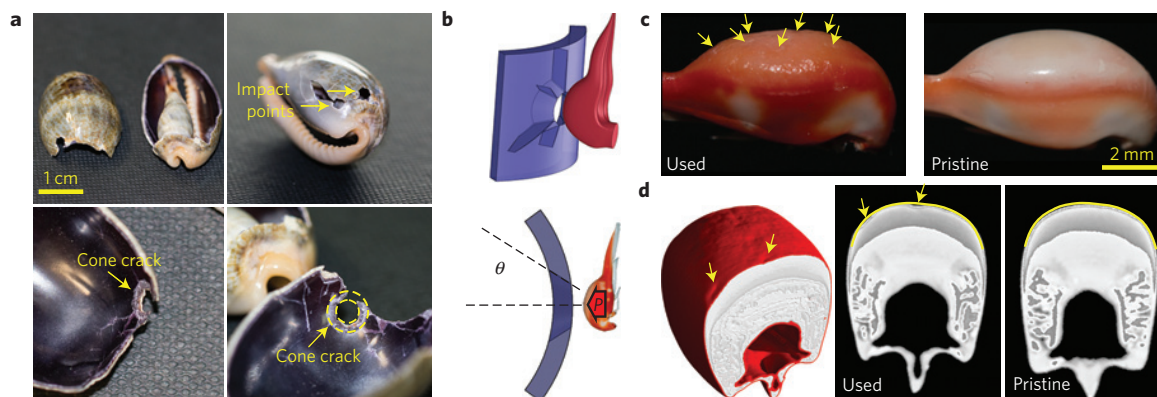
Figure 1 | Fractured shell impacted by a stomatopod dactyl club, and overview of dactyl clubs visualized by macro-photography and microCT scan.
a, Photographs of a fractured snail shell after impact from a stomatopod's dactyl club, showing the classical brittle cone cracks (Hertzian cracks) at the impact points that led to macroscopic fracture. **b**, Schematic illustration of the impact depicting the cone shape fracture pattern in the snail shell.
c, Macro-photographs of a used and a pristine dactyl club. Arrows indicate plastically eroded regions after repetitive impacts. **d**, MicroCT images of a used club (left) and cross-sections of a used and a pristine club (right).

the outer layers towards the inner (bulk) layers. In the vicinity of the free impact surface, the indentation response was distinctly anisotropic (Fig. 2d). Here, both the slope (elastic modulus) and the yield stress σ_y were higher in the zz (5.0 ± 0.1 GPa) than in the yy direction (3.5 ± 0.1 GPa). The anisotropic response was less marked further inside the outer layers, and was not observed in the softer bulk layers (Fig. 2d). Quantitatively, σ_y decreased to 2.1 ± 0.1 GPa (zz direction) and to 1.6 ± 0.2 GPa (yy directions) near the interface with the inner region. Within the inner layers, the indentation stresses were much lower and remained below 1.0 GPa. In addition, the elastic–plastic transition became less obvious, possibly because surface yielding was initiated early at very low contact depth, even though a relatively large tip radius was used.

Dental enamel is one of the few biomineralized hard tissues for which indentation stress–strain curves have been generated[13,14]. It is composed primarily of hydroxyapatite, which is chemically very similar to FAP from the dactyl club, making enamel a very convenient benchmark for comparison with the outer layers of the clubs. The indentation yield stress of enamel has been reported to be approximately 3 GPa, which is in the same range as the outermost layer of the club. We also carried out indentation measurements on the 'spearer' stomatopod species (Supplementary Fig. 3) and obtained a higher yield stress in the yy direction of 4.4 ± 0.3 GPa, which is consistent with the absence of the softer chitin organic phase in the outer layers of the spearer club[12]. The data are also in agreement with control experiments on an organic-free geologic FAP (Supplementary Fig. 4) where an indentation yield stress of close to 9 GPa was measured.

Under hydrated conditions (loading–unloading cycles, Fig. 2b, bottom curves and derived stress–strain curves, Fig. 2e) the mechanical contrast between the various layers became even more evident. Indeed, whereas the elastic–plastic behaviour of the outermost layer was moderately affected by hydration (yy direction, $\sigma_{y,hydrated} \approx 2.6 \pm 0.2$ GPa, $\sigma_{y,dry} \approx 3.5 \pm 0.1$ GPa), a sharp decrease in indentation stresses was noticed in the inner layers of the clubs, and these differences amplified as we move deeper into the bulk. Here, the indentation stress–strain response featured a strain-hardening type behaviour, with a rapid rise of stress when the indentation strain exceeded 20 to 30% (Fig. 2e, inset). As indentation curves exhibited large residual displacements on full unloading (Supplementary Fig. 5), strain hardening can be attributed to plastic deformation as opposed to an elastic mechanism that would involve very small residual displacements. Partially mineralized biocomposites and biopolymers are well

known to be strongly susceptible to hydration[1], and the inner layers of the dactyl clubs thus represent a compelling illustration of the contrast in mechanical properties between dry and hydrated conditions (Fig. 2e and Supplementary Fig. 3e,f) in these materials. It should be noted that in native conditions, the dense outer region acts as an efficient barrier against water infiltration; thus, the stress–strain response of the inner region in native conditions is likely to stand between the boundaries of the dry (Fig. 2c) and the fully hydrated curves (Fig. 2e).

Given the presence of a viscoelastic organic phase, we also verified the indentation response at higher loading rates under hydrated conditions. In the outer regions no differences were observed when the loading rate was increased up to 500-fold (Fig. 2f and Supplementary Fig. 6). In the layers just below the impact surface, the influence of loading rate remained negligible (minor shift of the curves towards the left, shown in red). In the bulk inner layers, a small loading rate effect was detected, which is consistent with the larger content of viscoelastic chitin in this region. However, the spatial location had the most dominant influence on the indentation response (compare the cyan green curves on the far right, measured on a location 50 μm away from the green (middle) curves). The impact velocities generated by the clubs at the contact point are extremely high (up to 20 m s^{-1}). To assess the level of strain rates that such high-velocity impacts generate in the club, we conducted dynamic finite element analysis (DFEA) simulations of the contact (Methods). We used a stiff steel target ($E = 200$ GPa) and separated the clubs into six distinct layers, with the constitutive laws of each layer obtained by fitting the indentation stress–strain curves presented in Fig. 2e (details of the simulation, Supplementary Note 2). At an impact velocity of 20 m s^{-1}, a maximum strain rate of 8.9×10^4 s^{-1} was reached in the innermost layers (Supplementary Fig. 7), which compared with a strain rate of the order of $\sim$3.3 s^{-1} for the highest loading rate (300 mN s^{-1}) in our experiments. Hence, it cannot be completely excluded that such high strain rates would affect the indentation response more significantly than observed in Fig. 2f. However, the maximum strain values in the innermost layers as obtained by simulation were about 10% (Supplementary Fig. 7), which according to the indentation stress–strain curves (Fig. 2e, inset) correspond to moderate stresses that are lower than 50 MPa. Thus, it is anticipated that strain-rate effects will not markedly affect the stress levels during an impact.

Micromechanisms of deformation

The stress–strain response of the inner layers was reminiscent of the compressive macroscopic response of lobster endocuticle[15],
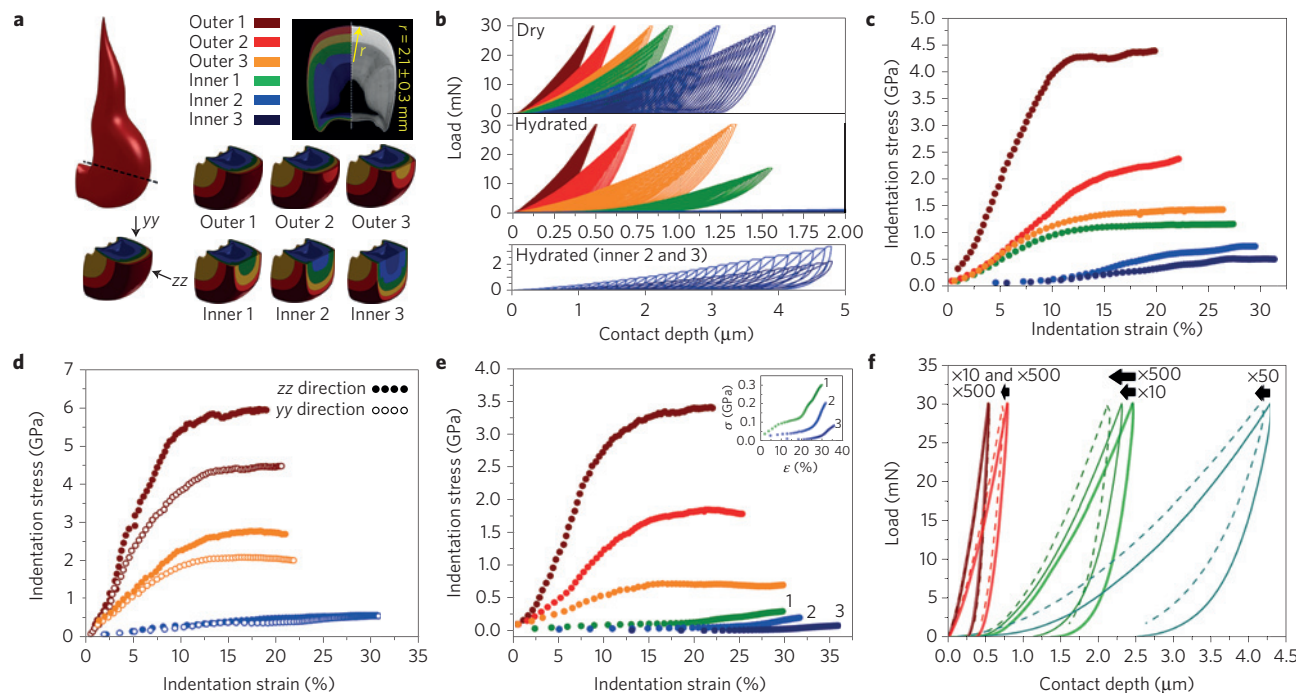
Figure 2 | Indentation response of the smasher dactyl club in distinct layers. a, Sample preparation for bi-directional probing of contact response, and schematic cross-section of a club, with colour coding representing the location where indentation studies were carried out (this colour coding is used throughout the manuscript). **b**, Partial loading–unloading curves in dry (top) and hydrated (middle and bottom) conditions. Full unloading was performed to obtain the contact depth and contact radius at a given peak load. The water content in hydrated conditions is 4–5 wt% in the outer layers and 10 wt% in the inner layers. **c**, Indentation stress–strain curves in dry conditions computed from the partial loading–unloading curves obtained in **b**. **d**, Indentation stress–strain curves (dry conditions) in the *yy* and *zz* directions depicted in **a**, illustrating the anisotropic response near the impact surface. **e**, Indentation stress–strain curves (hydrated conditions) computed from the partial loading–unloading curves obtained in **b**. The inset shows the strain-hardening behaviour of the inner layers. **f**, Loading–unloading curves (hydrated conditions) measured at 0.6 mN s^{-1} (thick line), 6 mN s^{-1} (thin lines), and 300 mN s^{-1} (dashed lines), illustrating the influence of loading rate in various regions of the clubs.

which is also a chitin/amorphous $CaCO_3$ composite exhibiting a helicoidal microstructure, and whose strain hardening in hydrated conditions has been attributed to densification of the pore channels running along the mineralized chitin fibrils. Such channels were also clearly present in the inner layers of the dactyl clubs (Fig. 3a), and we reasoned that strain hardening was also due to microchannel densification. We carried out high-load Hertzian indentation and devised a method to observe the plane directly under the contact point (Methods). The observations revealed clear morphological differences between the plastic region located directly beneath the indent compared with the surrounding elastic region. Whereas open channels were noticed in the elastic region, these pores were closed in the plastic region. The disparities between both areas were even more apparent at higher magnification (Fig. 3a-iii and iv), with no open channels in the plastic region. Further confirmation was achieved by conducting similar experiments using a sharp indenter (Fig. 3b). Here the maximum plastic strains are located near the side of the indenter pyramidal faces. Closed channels were detected in the plastic region and were unambiguously distinct from the open channels of the elastic region (Fig. 3b-ii to b-v). These observations thus corroborate the notion that microchannel densification plays a significant role in absorbing the impact energy. To the best of our knowledge, microscale densification has not previously been detected by depth-sensing nanoindentation.

Using the same methodology, we set out to elucidate the micromechanisms of deformation under blunt, native contacts of the impact surface (Fig. 3c). Such observations were thus conducted in the immediate vicinity of naturally impacted surfaces such as those shown in Fig. 1c,d. Two distinct regions could again be detected: a first region directly beneath the contact that was

heavily and irreversibly deformed during the high-load impact, and a second region away from the impact point that mostly sustained elastic deformation. In the latter, we observed an elongated columnar-like texture (middle to lower part of Fig. 3c-i), which could be better observed at higher magnification, both on the finely polished sample (Fig. 3c-iii) and on a fracture surface (Fig. 3c-iv). Previous investigations have established that the club's outermost layers consist of oriented FAP rods with a small amount of chitin[11,12]. In the heavily deformed region right beneath the contact, on the other hand, we observed misaligned FAP crystallites, visualized at higher magnification in Fig. 3c-ii. The microstructural morphology of this region is clearly distinct from the elastic region (compare with Fig. 3c-iii). These observations indicated that the FAP crystallites were subjected to intense submicrometre sliding and rotation, triggered by shear-band localization of the contact stress field[16]. For better visualization, we drew the preferred orientation of FAP crystallites detected in the plastic region on high-magnification field-emission scanning electron microscopy (FESEM) images (Fig. 3c-v, lower right panel), which compellingly illustrates the rearrangement of FAP crystallites in the plastic region. Further quantification of the crystallite orientation shown in Fig. 3c-ii and c-iii was carried out by image analysis with the ImageJ software (Supplementary Fig. 8a,b). In the elastic region, we observed that most FAP crystallites were oriented at 60° with respect to the horizontal axis of the image. In the heavily deformed region, on the other hand, the crystallites exhibited a much broader orientation distribution with many crystallites oriented in the range −20 to +20°. We then verified whether FAP crystallite sliding and rotation led to localized damage by conducting a series of indents in both regions (aligned and misaligned crystallites). We found no statistically significant differences for the
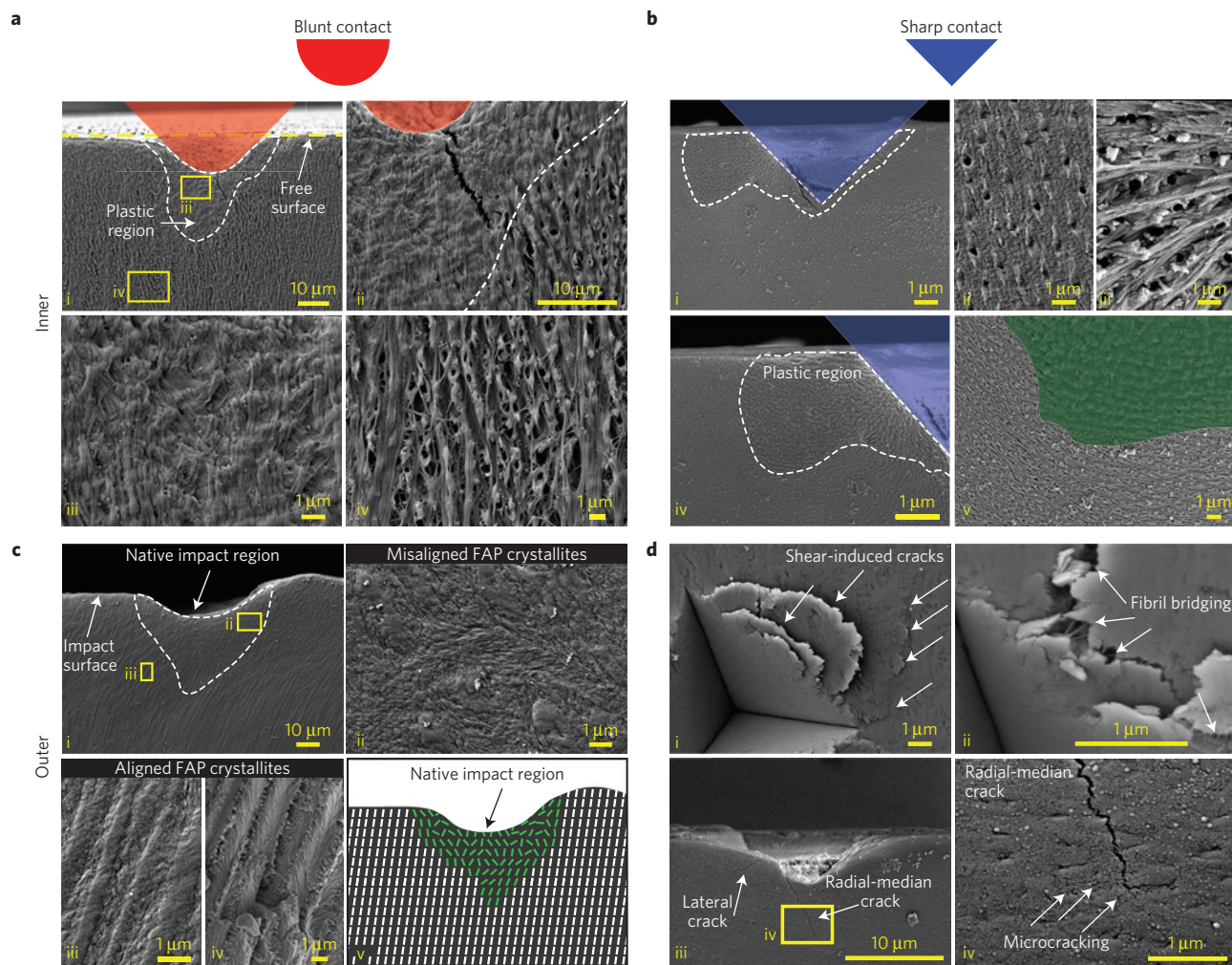
Figure 3 | Contact deformation and damage mechanisms of the dactyl clubs revealed by post-indentation FESEM observations of the planes beneath the contact points. a, Blunt contact, inner layers: (i) low-magnification micrograph illustrating both the plastic and elastic regions; (ii) higher-magnification micrograph depicting the elastic–plastic boundary; (iii) and (iv) high-magnification micrographs of closed channels in the plastic region and open channels in the elastic region, respectively, illustrating microchannel densification under contact. **b**, Sharp contact, inner layers: (i) low-magnification micrograph illustrating the plastic region near the sharp indenter edge and the surrounding elastic region; (ii) and (iii) microchannels before indentation viewed under two different orientations; (iv) and (v) boundary between the plastic and the elastic regions, with green shading area in (v) representing the closed, densified structure. **c**, Native impact blunt contact, outermost layer: (i) low-magnification micrograph comprising both the plastic and the elastic regions; (ii) high-magnification micrograph of the plastic region near the contact revealing highly misaligned FAP crystallites; (iii) high magnification of the elastic region showing the textured structure of FAP crystallites; (iv) fracture surface of the impact region (undeformed sample), confirming the textured structure of FAP; (v) schematic of misaligned FAP crystallites near the contact point, drawn by following the contour of actual crystallites on high-magnification micrographs (quantification of crystallite orientation is shown in Supplementary Fig. 8). **d**, Sharp contact, outer layers: (i) top view of shear-induced lateral cracks emerging on the free surface; (ii) high magnification of an indent corner, revealing fibril bridging between the two sides of a lateral crack; (iii) low-magnification side view showing lateral and radial-median cracks nucleated by the sharp contact; (iv) high-magnification micrograph of the radial crack tip region, showing the formation of a microcracking process zone surrounding the main crack.

average elastic modulus of both regions (Supplementary Fig. 8c,d). We also evaluated the relative contribution of plastic dissipation (W_p) to the total contact energy ($W_p + W_e$), where W_e is the elastic energy (Supplementary Fig. 9). We found that in the outermost layer 20 to 25% of the total contact energy was dissipated by plastic yielding. Plastic dissipation was slightly higher in the next outer layer (30–35%) and reached up to 50% in the inner layers, indicating that microchannel densification could absorb larger relative amounts of contact energy.

Indentation fracture

To complement our understanding of the dactyl club damage tolerance, we investigated the fracture response of the dactyl club using indentation fracture. For this purpose, we selected the sharp

cube-corner indenter geometry for its ability to nucleate cracks, for a given material, at much lower external loads than the standard Berkovich geometry[17,18]. Indents were performed across a wide range of peak loads (from 10 mN to 3,000 mN, Fig. 4). In the outer layers of the club, the crack nucleation load P_c as detected by the first pop-in event on the load–displacement curve was between 15 and 25 mN. This compared to P_c values as low as 4–8 mN on a control geologic FAP sample (Fig. 5). In the inner layers, on the other hand, no cracks nucleated up to values as high as 3,000 mN, which corresponded to the maximum load compatible with the club size (Fig. 4d). Post-indentation FESEM micrographs revealed the initiation of three cracks in the immediate vicinity of the indent (Fig. 4c). A close inspection of load–displacement curves associated with the indent patterns shown in Fig. 4c revealed
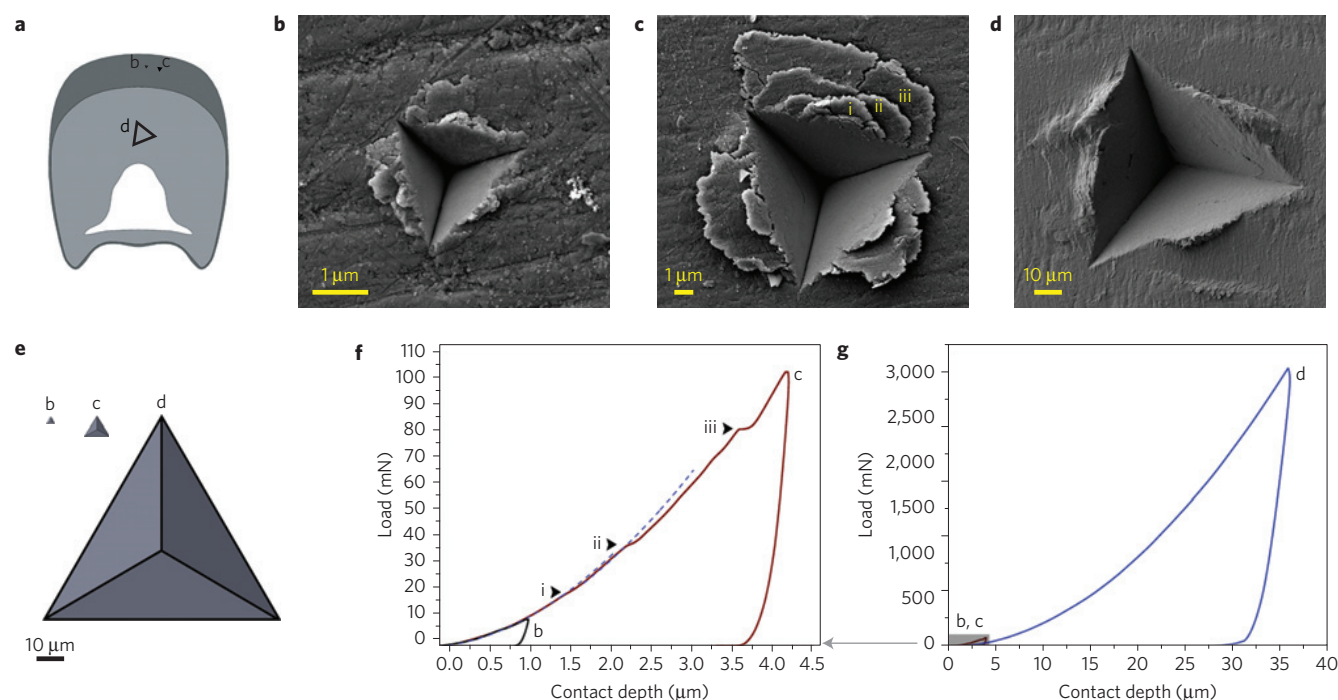
Figure 4 | Multi-scale indentation fracture studies of the dactyl clubs. a, Schematic of indent locations. **b–d**, Post-indentation FESEM micrographs corresponding to the locations shown in **a**. Outer layer, peak load of 10 mN (**b**); outer layer, peak load of 100 mN (**c**); inner layer, peak load of 3,000 mN (**d**). **e**, Characteristic indent sizes shown in **b–d** at the same scale. **f**, Indentation curves corresponding to indents in **b** and **c**. Dashed lines are fitting of the initial elastic region, with deviation from the experimental curves used to detect pop-in events (shear-induced cracks associated with the pop-in events shown in **c**). **g**, High-load (3,000 mN) indentation curve of the dactyl club inner region, illustrating no pop-in events. The maximum loads from **b** and **c** are shown for comparison.

three pop-in events (Fig. 4f), as detected by discontinuities in the loading curve, which can be attributed to perturbations beneath the contact point[19]. At low loads, the pop-in events were precisely identified by fitting the initial portion of the curve with a power-law relationship and by comparing it with the experimental curve. At higher loads, the pop-in events were evident from the curves. These correlations strongly suggest that the pop-in events were due to microcracking around the indents. However, in comparison with classical radial cracks that are formed in purely brittle materials[16], the crack patterns indicated shear-induced cracking, nucleated by shear-band localization generated by the contact stress field. We probed the damage micromechanisms at sharp indents (Fig. 3d) and identified at least two types of toughening mechanism by observing the crack tip regions. First, we detected evidence of chitin fibril bridging at shear-induced crack corners (Fig. 3d-ii). Second, we also observed the formation of a process zone consisting of microcracks surrounding the main radial crack (Fig. 3d-iv). Both mechanisms parallel key dissipative energy processes identified in bone[20,21], indicating a similar synergistic action of multiple toughening mechanisms in the mantis shrimp's clubs.

To quantify the released energy during crack events at the indentation edges, we correlated the pop-in events with the energy released during cracking. For sharp contact indentation, where yielding can be followed by cracking events at the contact point[22], the area under a loading–unloading cycle corresponds to the sum of two energies: the energy dissipated by plastic yielding and the elastic energy released during cracking events (a third contribution, the elastic energy restored during the unloading portion of the cycle, can be considered negligible here). Thus, if no cracking occurs, 100% of the input energy is dissipated by plastic yielding, and this value decreases when cracks nucleate from the contact point and propagate. This quantity can be regarded as a damage index (d_i), which is related to the capacity to absorb contact energy by

yielding before cracking. The area under pop-in events due to the elastic energy released during cracking was integrated as illustrated in Fig. 5a, which was done for the outer layer, an FAP geologic control, and the inner region. The total energy released during cracking as a function of the applied load was also computed (Fig. 5b). For instance, at an applied load of 100 mN, the released elastic energy by cracking relative to the total energy during the indentation process ($1 - d_i$) was $45 \pm 4\%$ for FAP and $12 \pm 3\%$ for the club outer layer. In other words, the club outer layer was able to absorb almost four times more contact energy by yielding before cracking in comparison with the geologic FAP crystal. Figure 5b also indicates that the released energy during crack propagation exhibited a power-law dependence with the load in FAP, whereas for the club outer layer the correlation was almost linear and lower in absolute values than in FAP. A slightly higher absorption energy was also noticed in the *zz* direction (Supplementary Fig. 10a). For the inner layer, $1 - d_i = 0 \pm 0\%$ for the entire applied load range, meaning that no cracking occurred during the indentation process. Hence, a high amount of plastic yielding occurred in the bulk region before any cracks were nucleated, which is not surprising considering its strain-hardening indentation stress–strain response. To further quantify damage localization, the high-load indents were inspected with FESEM (Fig. 5c–e) and the results were compared with the control geologic FAP crystal. We found that the ratio of damage size (r_d) to indent size (r_i) in the outer layer of the dactyl club sample was about 50% smaller compared with the FAP crystal sample (1.50 ± 0.04 and 2.90 ± 0.34, respectively). For the inner layer no crack or external damage was observed around the indents, which also corroborated the indentation curves for this layer (Fig. 5a,b, blue curves). We also assessed loading rate effects during sharp indentation, and found no statistically significant differences on the indentation profiles and released energies for both the inner and the outer layers (Supplementary Fig. 10b–d).
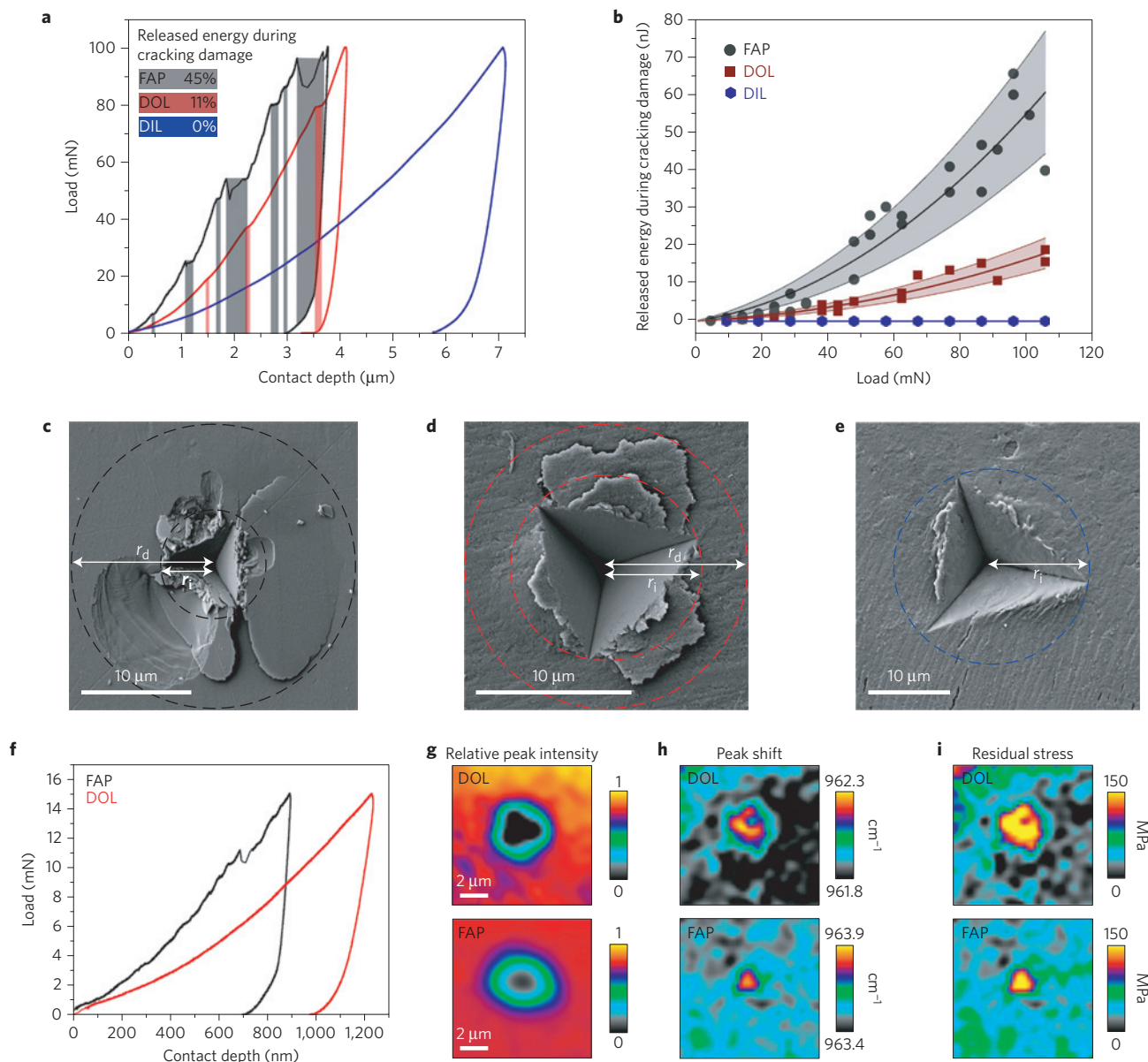
Figure 5 | Sharp contact indentation and residual stress fields in the dactyl clubs, and comparison with geologic FAP. a, Indentation curves for FAP, the dactyl club outer layer (DOL) and the dactyl club inner layer (DIL). The shaded areas under the curves correspond to the energy released during a cracking event at the contact point. **b**, Released energy versus indentation load for the 3 samples. **c–e**, Post-indentation FESEM micrographs of FAP (**c**), DOL (**d**) and DIL (**e**). **f**, Indentation curves on FAP and DOL samples used for visualization of residual stress fields. **g–i**, Raman mapping for visualization of residual stress fields around indents of FAP and DOL. Relative intensity of the ν_1 band of FAP (**g**); peak shift of the ν_1 band (**h**); and residual stress fields as computed from the relative peak intensity and peak shift (**i**).

Inhibition or delay of cracking at sharp contacts in ceramics can be attributed to the ability of the material to undergo localized shear deformation[23]. This mechanism gives rise to contact stress redistribution under the contact point[16,23], in principle resulting in the formation of a significant residual stress field. To test that this mechanism applies to the dactyl clubs, we used high-resolution Raman microspectroscopy to detect the shift of the ν_1 band of FAP (Fig. 5g–i) around the indents, according to a methodology developed previously[14]. The experiments were performed on indents generated with a 15 mN peak load, on both the outer layer of the dactyl club and a FAP geologic crystal (Fig. 5f). We observed that the residual stress area in the dactyl club outer layer was almost four times larger than in FAP (Fig. 5i). This further confirmed that in the geologic FAP a high fraction of indent energy is released by cracking, thus leaving a small residual stress field.

In the club outer layer, on the other hand, a larger yielding zone developed around the contact point, building up a complex residual stress field where a high amount of contact energy was absorbed.

Quasi-plasticity versus brittle fracture

The results from both elastic–plastic (blunt Hertzian contact) and fracture (sharp contact) investigations provide clear insight into the overall damage tolerance of the club. The indentation process—and thus resistance to contact—of hard materials represents a close competition between yielding and cracking beneath the contact point[22,24]. For blunt contacts, the following brittleness index ratio has been suggested[25]:

$$\frac{P_\gamma}{P_c} = \left(\frac{D}{A}\right)\left(\frac{H}{E'}\right)\left(\frac{H}{T}\right)^2 r'$$

where P_y and P_c are the external loads to initiate yielding or cracking, respectively, D and A are constants equal to 0.848 and 8.63×10^3, respectively, H is the hardness, E' is the effective modulus, T' is fracture toughness, and r' is the contact radius of curvature. When $P_y/P_c > 1$, the contact response of the material is brittle, whereas if $P_y/P_c < 1$ the behaviour is referred to as quasi-plastic. Therefore, for quasi-plastic materials, significant yielding beneath the contact precedes the nucleation and rapid propagation of a large crack triggered by the Hertzian stress field[16], with yielding occurring along localized shear bands. Using the values of H, E' and a contact radius of $10\,\mu m$, we obtain for the outer layer a P_y/P_c ratio of about 4.9×10^{-4} and 3.9×10^{-4} in the zz and the yy directions, respectively, in both dry and hydrated conditions. This strongly suggests that the critical load for brittle cone fracture at the contact point is much larger than the critical load for quasi-plasticity. Thus, incipient quasi-plasticity occurs within a confined subsurface yield zone governed by the shear components of the Hertzian stress field[25,26]. Confined yield beneath the contact point in impact resistant, quasi-plastic ceramics can be achieved by preparing coarse grain microstructures, with grains typically larger than one micrometre[16,27]. In stark contrast, the dactyl club's outer layer is made of FAP nanorods, and our post-impact observations (Fig. 3c) reveal that confined yield is achieved by a distinct deformation micromechanism consisting of submicrometre intercrystalline sliding and rotation of initially oriented FAP nanorods, a mechanism that is gradually building up during each impact and which we are not aware of in other hard biological composites. This behaviour is probably facilitated by the viscoelastic nature of the organic phase surrounding the FAP crystalline rods, similar to axial micro-tablet sliding[3,28] and nanograin rotation[29] observed in nacre.

Furthermore, there also exists a transition radius r^*, corresponding to $P_y/P_c = 1$, above which the response shifts from quasi-plastic to brittle. This transition radius for the outermost layer of the dactyl club is found to be about 20 mm (zz direction). As the average radius of curvature of the clubs is 2.1 ± 0.3 mm (Fig. 2a, $n = 12$), a key implication is that during impact on hard shells the macroscopic size of the clubs precludes the formation of cone cracks in the clubs. On the other hand, such catastrophic cracks will be formed on the prey's hard shells (Fig. 1). We also calculated the transition radius for the spearer species, and obtained a value of 6 mm. Interestingly, the curvature radius of the impact (apex) region in the spearer is $30\,\mu m$ (Supplementary Fig. 3b), again much smaller than the transition radius, suggesting a curvature that prevents catastrophic cracking at the impact point in all mantis shrimp species.

Mantis shrimps deliver very high impact velocities in the wild, which generate loading rates at the contact point that are larger than the highest loading rates imposed in our experiments. Strain-rate effects are well known to influence the mechanical response of structural materials, especially ductile metallic alloys or structural polymers[30]. In the extreme case, the so-called ductile-to-brittle transition occurs as the strain rate increases, with concomitant changes in the dominant micromechanisms of failure[30]. We reason that such ductile-to-brittle transition is unlikely in the dactyl clubs. Indeed, microplasticity under native blunt contact was clearly identified in native specimens (Figs 1d and 3c), which would be incompatible with a brittle response. We did not observe any catastrophic brittle fracture in the clubs, nor has it been documented in the past. The dactyl club represents a central component of the evolutionary survival of stomatopods and must have thus evolved to prevent such a ductile-to-brittle transition, which would completely undermine their hunting strategies. The inner layers, on the other hand, must exhibit a stronger strain-rate dependence given their higher content of viscoelastic phase. Although our DFEA simulations (Supplementary Fig. 7) indicate that the maximum strain rates attained in the inner layers following impact are higher than those imposed in our indentation experiments, the maximum strains in these layers

correspond to relatively low stresses, where strain-rate effects are expected to remain moderate. Nevertheless, it remains to be determined to what extent higher loading rates than employed in our indentation experiments would affect the stress–strain response, in particular in the inner layers.

Outlook

To the best of our knowledge, indentation stress–strain curves with micrometre spatial resolution on multilayer biological composites have previously not been reported, especially in hydrated conditions. In addition, our multiscale sharp-contact indentation measurements provide quantitative insights into the relative contributions of energy dissipated by yielding or released by cracking, respectively. Together, these data indicate that the outer region of the club exhibits a graded, quasi-plastic compressive response, resulting in significant energy dissipation by localized yielding before shear-induced circumferential cracks are nucleated. Mechanical anisotropy is largely restricted to the impact surface in the form of enhanced resistance against yielding in the direction perpendicular to the impact surface. On the other hand, the inner layers composed of chitin and amorphous minerals exhibit strain hardening, with lower compressive yield strengths but much higher yield strains, a design that is efficient in absorbing additional impact energy. The deformation mechanisms associated with each response are markedly different. Whereas quasi-plasticity occurs by localized interfacial sliding and gradual rotation of apatite nanorods during consecutive impacts, strain hardening results from microchannel densification. We conclude that the macroscopic size of the clubs is smaller than the transition radius of a blunt contact above which the contact mechanics response switches from quasi-plastic to brittle, a key criterion in preventing catastrophic macroscopic failure of the clubs during impact against prey. These findings provide useful guidelines for designing synthetic multi-material structures that must resist repetitive impact loading: a compromise in absolute hardness and stiffness values near the impact surface would be beneficial through the incorporation of a residual soft phase that can promote localized interfacial sliding and rotation of the initially textured hard phase, in turn leading to a quasi-plastic response at the impact point. Within the bulk of such components, on the other hand, the use of materials with strain-hardening response through micro-densification would provide additional mechanical dissipation.

Methods

Methods and any associated references are available in the online version of the paper.

References

1. Chen, P. Y., McKittrick, J. & Meyers, M. A. Biological materials: Functional adaptations and bioinspired designs. *Prog. Mater. Sci.* **57,** 1492–1704 (2012).
2. Amini, S. & Miserez, A. Wear and abrasion resistance selection maps of biological materials. *Acta Biomater.* **9,** 7895–7907 (2013).
3. Barthelat, F. & Espinosa, H. D. An experimental investigation of deformation and fracture of nacre-mother of pearl. *Exp. Mech.* **47,** 311–324 (2007).
4. Kamat, S., Su, X., Ballarini, R. & Heuer, A. H. Structural basis for the fracture toughness of the shell of the conch *Strombus gigas. Nature* **405,** 1036–1040 (2000).
5. Li, L. & Ortiz, C. Pervasive nanoscale deformation twinning as a catalyst for efficient energy dissipation in a bioceramic armour. *Nature Mater.* **13,** 501–507 (2014).
6. Bruet, B. J. B., Song, J., Boyce, M. C. & Ortiz, C. Materials design principles of ancient fish armour. *Nature Mater.* **748**–756 (2008).
7. Yao, H. *et al.* Protection mechanisms of the iron-plated armor of a deep-sea hydrothermal vent gastropod. *Proc. Natl Acad. Sci. USA* **107,** 987–992 (2010).
8. Munch, E. *et al.* Tough, bio-inspired hybrid materials. *Science* **322,** 1516–1520 (2008).

7

9. Studart, A. Towards high-performance bioinspired composites. *Adv. Mater.* **24,** 5024–5044 (2012).
10. Thoen, H. H., How, M. J., Chiou, T-H. & Marshall, J. A different form of color vision in Mantis shrimp. *Science* **343,** 411–413 (2014).
11. Weaver, J. C. *et al.* The stomatopod dactyl club: A formidable damage-tolerant biological hammer. *Science* **336,** 1275–1280 (2012).
12. Amini, S. *et al.* Textured fluorapatite bonded to calcium sulphate strengthen stomatopod raptorial appendages. *Nature Commun.* **5,** 3187 (2014).
13. He, L. H., Fujisawa, N. & Swain, M. V. Elastic modulus and stress–strain response of human enamel by nanoindentation. *Biomaterials* **27,** 4388–4398 (2006).
14. He, L. H. & Swain, M. V. Nanoindentation derived stress–strain properties of dental materials. *Den. Mater.* **23,** 814–821 (2007).
15. Sachs, C., Fabritius, H. & Raabe, D. Influence of microstructure on deformation anisotropy of mineralized cuticle from the lobster *Homarus americanus*. *J. Struct. Biol.* **161,** 120–132 (2008).
16. Lawn, B. Indentation of ceramics with spheres: A century after hertz. *J. Am. Ceram. Soc.* **81,** 1977–1994 (1998).
17. Morris, D. J. & Cook, R. F. *In situ* cube-corner indentation of soda-lime glass and fused silica. *J. Am. Ceram. Soc.* **87,** 1494–1501 (2004).
18. Miserez, A. *et al.* Effects of laminate architecture on fracture resistance of sponge biosilica: Lessons from Nature. *Adv. Funct. Mater.* **18,** 1–8 (2008).
19. Schuh, C. A. Nanoindentation studies of materials. *Mater. Today* **9,** 32–40 (2006).
20. Launey, M. E., Chen, P-Y. & Ritchie, R. O. Mechanistic aspects of the fracture toughness of elk antler bone. *Acta Biomater.* **6,** 1505–1514 (2010).
21. Wang, R. & Gupta, H. S. Deformation and fracture mechanisms of bone and nacre. *Annu. Rev. Mater. Res.* **2011,** 41–73 (2011).
22. Lawn, B. *Fracture of Brittle Solids* 2nd edn (Cambridge Univ. Press, 1993).
23. Wang, X., Padture, N. P. & Tanaka, H. Contact-damage-resistant ceramic/single-wall carbon nanotubes and ceramic/graphite composites. *Nature Mater.* **3,** 539–544 (2004).
24. Zok, F. & Miserez, A. Property maps for abrasion resistance of materials. *Acta Mater.* **55,** 6365–6371 (2007).
25. Rhee, Y-W., Kim, H-W., Deng, Y. & Lawn, B. R. Brittle fracture versus quasi plasticity in ceramics: A simple predictive index. *J. Am. Ceram. Soc.* **84,** 561–565 (2001).
26. Deng, Y., Lawn, B. R. & Lloyd, I. K. Characterization of damage modes in dental ceramic bilayer structures. *J. Biomed. Mater. Res.* **63,** 137–145 (2002).
27. Guiberteau, F., Padture, N. P. & Lawn, B. R. Effect of grain size on Hertzian contact damage in alumina. *J. Am. Ceram. Soc.* **77,** 1825–1831 (1994).
28. Barthelat, F., Tang, H., Zavattieri, P. D., Li, C-M. & Espinosa, H. D. On the mechanics of mother-of-pearl: A key feature in the material hierarchical structure. *J. Mech. Phys. Solids* **55,** 306–337 (2007).
29. Li, X., Xu, Z-H. & Wang, R. *In situ* observation of nanograin rotation and deformation in nacre. *Nano Lett.* **6,** 2301–2304 (2006).
30. Meyers, M. A. *Dynamic Behavior of Materials* 323–381 (John Wiley, 1994).

Author contributions

S.A. conducted all experiments and DFEA simulations, and performed all data analysis. M.T. helped conduct nanoindentation experiments, DFEA simulations, and Raman spectroscopy data analysis. S.I. advised on Hertzian indentation experiments, supervised DFEA simulations, and provided editorial comments. A.M. designed and supervised the study. A.M. and S.A. wrote the paper with input from all authors.

Additional information

Supplementary information is available in the online version of the paper. Reprints and permissions information is available online at www.nature.com/reprints. Correspondence and requests for materials should be addressed to A.M.

Competing financial interests

The authors declare no competing financial interests.

Methods

Materials. Club samples were dissected from stomatopods (*Odontodactylus scyllarus*) acquired from commercial sources in Singapore. The clubs were kept at −80 °C before cutting and mounting. The samples were embedded in an acrylic cold mounting resin (ClaroCit, Struers), sectioned using a linear precision diamond saw IsoMet 4000 (Buehler), ground with P1200/4000-grade SiC paper, and finally polished with 1 and 0.25 µm diamond paste. A 5 min ultrasonic bath was used to remove diamond paste particles and polishing debris from the samples surfaces after each step.

Field-emission scanning electron microscopy (FESEM). Samples were examined with a FESEM (JEOL, 7600F) at a low 5 kV accelerating voltage. To prevent surface charging, the samples were coated with 5 nm Pt and a lower secondary electron detector (LEI) was used.

Optical and microCT imaging. Used and pristine dactyl clubs were imaged using an EOS 700D camera equipped with an EF 100 macro lens (Canon). The microCT micrographs were imaged using an inspeXio SMX-90CT Plus (Shimadzu) with a 90 kV voltage and voxel size 0.012 mm pix^{-1}. The three-dimensional model was rendered using VGStudio Max.

Observation of deformation and fracture mechanisms. High-load indents were placed with both blunt and sharp tips. Next, the indented samples were polished with a fine (40 nm) colloidal silica suspension along a plane oriented parallel to the loading axis, until the plane located directly underneath the indenter axis was exposed. The samples were thoroughly inspected at regular intervals by optical microscopy to avoid over-polishing. Once the plane parallel to the indenter axis was reached, FESEM observations were conducted on the deformed zones directly beneath the indents. Similar procedures were carried out on native surfaces whose visual inspection (Fig. 1c) revealed intense impact by the animal.

Nanoindentation. Indentation studies were performed using a Triboindenter TI-950 nanomechanical tester (Hysitron). Hertzian contact studies were performed using a 30 mN standard transducer with a 10 µm nominal cono-spherical fluid cell tip at loading rates ranging from 0.5 to 300 mN s^{-1}. For the dried conditions, 80 partial loading–unloading cycles were conducted from 50 µN up to 30 mN. For the hydrated conditions, a custom-made fluid cell was filled with water. To minimize the drift effects due to long-term loading–unloading cycles, the tip was engaged with the specimen in the imaging mode for 30 to 40 min before each experiment. Eighty partial loading–unloading cycles from 10 µN to 30 mN were conducted. Details of the data analysis for the Hertzian contact studies are provided in Supplementary Fig. 2 and Supplementary Note 1. For the indentation fracture studies, a 10 N high-load transducer was used, and all indents were performed with a cube-corner diamond tip at loading rates ranging from 0.5 to 100 mN s^{-1}.

For multi-directional indentation studies, the response of the free surface was first obtained in the zz direction, which was possible because the free surface exhibited a remarkably small surface roughness (in the range of 20–30 nm). Next the sample was polished such that the cross-sectional plane perpendicular to the free impact surface was exposed (as depicted in Fig. 2a). A series of loading–unloading cycles was conducted on this plane in the yy direction at well-defined distances (y_0, y_1, y_2 and so on), starting from the outermost layer ($y_0 = 0$). The samples were then finely polished normal to the zz direction from the free impact surface (thus, exposing a plane perpendicular to the previous polishing plane) according to the y_i distances previously defined. After each polishing step, indentation cycles were conducted, such that the stress–strain response in the zz direction was obtained at distances equivalent to the measurements conducted in the yy direction, but orthogonal to the latter. Once a set of indentation cycles was obtained in the zz direction, the procedure was repeated for the location y_{i+1}.

Raman spectroscopy. High-resolution Raman imaging of post-indentation residual stress fields was obtained by using a confocal Raman microscope (alpha300, WITec) equipped with a 633 nm laser source and a ×20 objective lens. An integration time of 0.5 s and pixel size 0.3 µm were used for acquisition. The spectrometer was calibrated using a silicon wafer sample. WITec Project 2.08 was used for filtering, analysis and plotting the data.

Dynamic finite element analysis (DFEA). To simulate the impact event between the dactyl club and a stiff target, a two-dimensional planar model of the club and target (stainless-steel barrier) was designed and analysed using the commercial finite element software Abaqus/Explicit 6.13. The constitutive laws response of the different layers (Fig. 2) of the club was obtained by fitting the experimental Hertzian stress–strain curves in hydrated conditions. The contact between the club and target was defined as frictionless (tangential) and hard (normal). The target was fully constrained and a 20 m s^{-1} velocity was applied to the club along the normal direction. Further details are provided in Supplementary Note 2.

Data analysis and plotting. Statistical analysis and data plotting were done using the OriginPro 9.1 software. Polynomial curve fitting (second order) was used for detecting shallow-depth pop-in events (Fig. 4f). A total number 24 dactyl club samples were tested in the entire study. All nanoindentation samples were conducted on moulted, fully mineralized clubs that also exhibited fully formed inner layers. The data shown in Supplementary Fig. 8 were acquired near naturally impacted points. All conditions for indentation studies (spatial location, hydrated and dry, orientation, and loading rates) were repeated three times and all curves presented are representative for each set of conditions.